Title
Cathode Chemistries and Electrode Parameters Affecting the Fast Charging Performance of Li-Ion Batteries

Journal
Journal of Electrochemical Energy Conversion and Storage, 17(2)

ISSN
2381-6910

Authors
Zhao, Rui
Liu, Jie
Ma, Fai

Publication Date
2020-05-01

DOI
10.1115/1.4045567

Peer reviewed

Cathode Chemistries and Electrode Parameters Affecting the Fast Charging Performance of Li-Ion Batteries

Rui Zhao
Department of Mechanical Engineering,
University of California at Berkeley,
Berkeley, CA 94720
e-mail: ruizhao@berkeley.edu

Jie Liu[1]
Department of Mechanical and Aerospace Engineering,
Carleton University,
Ottawa K1S 5B6, ON, Canada
e-mails: Jie.liu@carleton.ca;
jliu@mae.carleton.ca

Fai Ma
Department of Mechanical Engineering,
University of California at Berkeley,
Berkeley, CA 94720
e-mail: fma@berkeley.edu

Li-ion battery fast-charging technology plays an important role in popularizing electric vehicles (EV), which critically need a charging process that is as simple and quick as pumping fuel for conventional internal combustion engine vehicles. To ensure stable and safe fast charging of Li-ion battery, understanding the electrochemical and thermal behaviors of battery electrodes under high rate charges is crucial, since it provides insight into the limiting factors that restrict the battery from acquiring energy at high rates. In this work, charging simulations are performed on Li-ion batteries that use the $LiCoO_2$ (LCO), $LiMn_2O_4$ (LMO), and $LiFePO_4$ (LFP) as the cathodes. An electrochemical-thermal coupling model is first developed and experimentally validated on a 2.6Ah LCO based Li-ion battery and is then adjusted to study the LMO and LFP based batteries. LCO, LMO, and LFP based Li-ion batteries exhibited different thermal responses during charges due to their different entropy profiles, and results show that the entropy change of the LCO battery plays a positive role in alleviating its temperature rise during charges. Among the batteries, the LFP battery is difficult to be charged at high rates due to the charge transfer limitation caused by the low electrical conductivity of the LFP cathode, which, however, can be improved through doping or adding conductive additives. A parametric study is also performed by considering different electrode thicknesses and secondary particle sizes. It reveals that the concentration polarization at the electrode and particle levels can be weaken by using thin electrodes and small solid particles, respectively. These changes are helpful to mitigate the diffusion limitation and improve the performance of Li-ion batteries during high rate charges, but careful consideration should be taken when applying these changes since they can reduce the energy density of the batteries.
[DOI: 10.1115/1.4045567]

Keywords: Li-ion battery, fast charging, thermal behaviors, cathode materials, electrode parameters, batteries, electrochemical storage

1 Introduction

The market share of electric vehicles (EVs) is growing quickly each year as a result of the multiple advantages of EVs including low or zero greenhouse gas emission, low cost to run and maintain, as well as some policies and incentives issued by governments. The state-of-the-art Li-ion batteries outperform other types of secondary batteries in terms of the range, weight, and life and are mostly adopted in EV applications.

The capacity of battery packs increases from hybrid electric vehicles to plug-in hybrid electric vehicles to battery electric vehicles (BEVs), and they are a series of products upon achieving the final goal of zero-emission. To accelerate the shift to fully electric vehicles among general public, approaches should be taken to reduce the cost of the batteries, as well as to facilitate the use of the vehicles in terms of extending the range and shortening the charging time. In this matter, fast charging is one of the key technologies in achieving this goal [1–4]. To realize fast charging, not only super chargers are required to deliver high power outputs, the batteries should also have the capability to receive such high power safely and without material or performance degradation.

Fast charging may not affect batteries' life if most of the particles in the electrodes participate in the reactions, while the particles may crack and get damaged if only a small number of particles undertake the reactions, as Li et al. stated after observing thousands of electrode nanoparticles at different states of charges (SoCs) [5]. Furthermore, heterogeneous utilization of the active material associated with local electrolyte depletion during the fast charge of thick electrodes can trigger earlier degradation mechanisms, such as lithium plating within the graphite anode, resulting in capacity fade during cycling [6]. Several groups have proposed new or modified electrode materials specifically to address fast charging issue [7–9]. For example, novel $TiNb_2O_7$ (TNO) anodes were synthesized and demonstrated excellent high-rate capability on a 49Ah large-size Li-ion battery, 90% capacity can be charged in 6 min at 10 C [7]. Graphene nanosheets were uniformly dispersed onto $LiNi_{1/3}Co_{1/3}Mn_{1/3}O_2$ cathode to enhance its rate capability. It was found that by adding 1 wt% graphene nanosheets, the SoC of the full cell at the end of constant current charges can increase from 6.6% to 38.5% at 5 C [8]. By coating graphite anodes with Al_2O_3, CR2032 coin-type cells ($LiCoO_2$ served as the cathodes) showed improved rate capability than the cells with pristine graphite anodes during tests at charging rates between 1000 and 4000 mA g^{-1} (1 C is at 161 mA g^{-1}) [9]. Besides preparing novel and modified electrodes, simulations were also performed to identify the causes of fast-charging related side effects and help design healthy and fast-charging schemes and select appropriate electrode chemistries, operating temperature, and electrolyte and microstructure properties [10–14]. For example, von Luders et al. developed a physicochemical model to simulate the lithium plating and stripping behaviors of Li-ion batteries [15]. Subsequently, Song and Choe proposed a charging method that utilizes negative current to promote lithium striping, which allows the recovery of the plated lithium to reduce the capacity fading [16]. Colclasure et al. modeled that improved ionic transport

[1]Corresponding author.

Manuscript received August 14, 2019; final manuscript received November 4, 2019; published online December 2, 2019. Assoc. Editor: George Nelson.

properties, either with higher electrolyte conductivity and diffusivity or less tortuous electrode microstructures, can noticeably delay lithium plating and thus enable fast charging [6]. Viswanathan et al. analyzed the battery-level heat generation of Li-ion batteries consisting of different anode and cathode chemistries across the 0 to 100% state of charge range. They elucidated that the reversible heat plays a key role in affecting the thermal responses of Li-ion batteries and proposed that a suitable choice of cathode and anode can mitigate the thermal management issues for EVs [17].

To facilitate and deepen the understanding of the battery responses during fast charging at both the battery and electrochemical cell levels and to identify the factors that restrict the electrodes from acquiring lithium ions, an electrochemical-thermal coupling model is implemented in this paper to simulate the charging behaviors of Li-ion batteries. The model is first validated on a Li-ion battery that uses $LiCoO_2$ (LCO) cathodes (noted LCO battery in the following text). It is then employed to simulate the Li-ion batteries with $LiMn_2O_4$ (LMO) and $LiFePO_4$ (LFP) cathodes for comparison due to their different electrode parameters and entropy profiles. A sweep study is also carried out by using different realistic electrical conductivities for the LFP cathode to study how it affects the fast-charging process. Lithium plating and utilization of active materials, which are two indicators of the fast-charging quality, are then analyzed at the electrode level. By varying the electrode thickness and active particle size, the indicators are compared and discussed to help optimize the electrodes for achieving high energy density while maintaining fast charging ability.

2 Experimental Setup

A pouch-type high-drain LCO battery is used in this work to validate the model, and its specifications are given in Table 1. Two thermal-related tests are performed on the battery: one test is to determine the convective heat transfer coefficient at the battery surface, and the other test is to record the voltages and temperatures of the battery during charges for model validation. For both tests, the battery is placed in a sealed plastic container with internal dimensions of $150 \times 100 \times 50$ mm for creating a similar operating environment as in a battery case, and a k-type thermocouple is securely attached to the battery surface center using aluminum foil and Kapton tapes for temperature measurement at a frequency of 1 Hz through a Pico-08 Data Logger. In the first test, the battery is warmed up in a Thermo Scientific Oven (PR305225G) to 40 °C before placing back to a 24 °C room condition. The cooling curve of the battery is recorded and fitted with a simulation result to determine the convective heat transfer coefficient. In the second test, the battery is first fully discharged to a voltage of 3.0 V at a rate of 0.5 C using a battery analyzer (Energy Storage Instruments PCBA 5010-4). It is then charged at constant charging rates of 0.5 C, 1 C, and 3 C until the voltage reached 4.2 V.

3 Model Description

A pseudo-2D (P2D) electrochemical and 3D thermal coupling model is employed in this work to investigate the charging behaviors of Li-ion batteries with LCO, LMO, and LFP cathodes and electrode parameters. Graphite is employed as the anode material for all the simulations since it remains the most competitive active material of choice for the Li-ion battery anode when considering the cost, capacity, and voltage profile [18]. In the coupling model, for each time step, the heat generation rate calculated from the P2D electrochemical model is averaged over entire electrochemical cell and applied to the battery geometry excluding the tabs as the battery heat source in the 3D transient thermal model, while the averaged surface temperature obtained by the transient thermal model is, in turn, input to the electrochemical model to update the temperature-dependent properties. Figures 1(*a*) and 1(*b*) show the schematic geometries of the electrochemical cell and pouch battery used in the model. As illustrated in Fig. 1(*a*), during the charge process, the lithium ions deintercalate from the cathode materials and diffuse to the anode through the electrolyte phase, while the electrons generated during the reactions follow an opposite path through the external circuit to complete the electrochemical reactions.

Table 1 Specifications of the pouch-type high-drain battery

Parameters	Value
Capacity (Ah)	2.6
Nominal voltage (V)	3.7
Voltage range (V)	3.0–4.2
Maximum charge rate (C)	5
Maximum discharge rate (C)	50
Weight (g)	62
Length (mm)	118
Width (mm)	38
Thickness (mm)	5.2

3.1 Electrochemical Model. The electrochemical model is governed by the material and charge balance equations in electrolyte and electrode phases and the Bulter–Volmer equation, as summarized in Table 2 [19]. The boundary conditions used in the P2D electrochemical model are available in Ref. [19].

The overpotential η in the reaction current density equation (also known as the Bulter–Volmer equation) is defined as

$$\eta = \Phi_s - \Phi_e - U \tag{1}$$

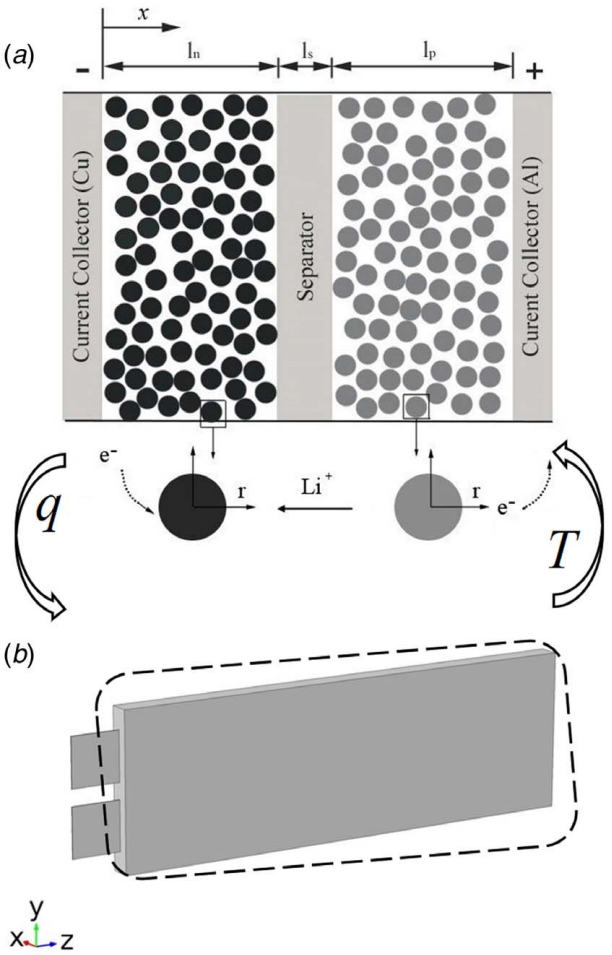

Fig. 1 Schematic geometries of the (*a*) electrochemical cell and (*b*) pouch battery used in the coupling model

Table 2 Equations in the electrochemical model

Conservation equations	
Material balance, electrolyte phase	$\varepsilon_e \frac{\partial c_e}{\partial t} = \frac{\partial}{\partial x}\left(D_e^{\text{eff}} \frac{\partial c_e}{\partial x}\right) + \frac{(1-t_+^0)}{F} j^{Li}$
Material balance, solid phase	$\frac{\partial c_s}{\partial t} = \frac{D_s}{r^2}\frac{\partial}{\partial r}\left(r^2 \frac{\partial c_s}{\partial r}\right)$
Charge balance, electrolyte phase	$-\left(k^{\text{eff}} \frac{\partial \Phi_e}{\partial x}\right) + \frac{2RT(1-t_+^0)}{F}\left(k^{\text{eff}} \frac{\partial(\ln c_e)}{\partial x}\right) = \mathrm{i_e}$
Charge balance, solid phase	$-\sigma^{\text{eff}} \frac{\partial \Phi_s}{\partial x} = \mathrm{i_s}$
Reaction current density	$j^{Li} = a_s i_0\left[\exp\left(\frac{0.5F}{RT}\eta\right) - \exp\left(-\frac{0.5F}{RT}\eta\right)\right]$
Effective electrolyte ionic diffusivity	$D_e^{\text{eff}} = D_e \varepsilon_e^{1.5}$
Effective electrolyte ionic conductivity	$k^{\text{eff}} = k\varepsilon_e^{1.5}$
Effective solid-phase electrical conductivity	$\sigma^{\text{eff}} = \sigma\varepsilon_s$
Specific interfacial surface area	$a_s = \frac{3\varepsilon_s}{R_s}$

where Φ_s and Φ_e are the electric potentials of solid phase and electrolyte phases, respectively. U is the equilibrium potential. The equilibrium potentials for graphite anode and LCO, LMO, and LFP cathodes are selected from previous literatures and plotted in Fig. 2(*a*) [20–24].

In the work from Viswanathan et al. [17], the entropy changes are given at different state of charges (SoCs) because the electrochemical model was not considered, and the heat generation rates were calculated on the battery level at different SoCs. In this work, the equilibrium potential and entropy changes are plotted against the filling fraction (or stoichiometry) instead of SoCs since the electrochemical reactions are taken into consideration in the model. The filling fraction is the ratio of lithium-ion concentration in electrode particles over the maximum fillable concentration, and it can be expressed as x and y in anode and cathode, respectively. For example, during the charge process, the reactions taking place in two electrodes can be expressed as

$$Li_yCoO_2 \overset{charge}{\rightarrow} Li_{y-x}CoO_2 + xLi_x + xe^- \tag{2}$$

$$C_6 + xLi^+ + xe^- \overset{charge}{\rightarrow} Li_xC_6 \tag{3}$$

Figure 2(*a*) shows that the three cathodes work in different ranges of filling fractions. Their physical properties used in the model are also different, as summarized in Table 3. Parameters used in the model are selected from the available literature to ensure the accuracy of the simulation results. The electrolyte ionic conductivity (k) is salt concentration-dependent, and the data used in this paper are based on the work from Doyle et al. [25].

In this work, the tested LCO battery serves as the reference battery. Its anode, cathode, separator, and current collector thicknesses are measured and used in the simulation to estimate the initial lithium-ion filling fraction in anode and LCO cathode during the charge process. Specifically, we first set the maximum solid-phase concentrations in anode and cathode same as the literature. Following that, voltage curves are simulated by using different initial filling fractions, which are compared with the measured voltage curves to determine the closest stoichiometry. To have a reasonable comparison of LCO, LMO, and LFP batteries, the thicknesses of the LMO and LFP cathode are adjusted to ensure the lithium-ion filling fraction ranges in the graphite anode (i.e., from x_1 to x_2 in Fig. 2(*a*)) as well as the inward electrode current density (9.8 A m^{-2} at 1 C) are the same with the reference battery.

LFP has been known to be a poor conductor, and this property is highly dependent on many factors, such as carbon content, carbon coating quality, calendaring, and doping materials [38–40]. Therefore, as shown in Table 3, three electrical conductivities of 0.005, 0.01, and 0.5 S m^{-1} are selected for LFP cathode after a review of relevant literature articles [31–33], which shows that an electrical conductivity between 0.001 and 1 S m^{-1} is reasonable.

An Arrhenius equation describes the temperature dependence of the exchange current density, solid and electrolyte phase diffusion coefficients, as well as the electrolyte phase conductivity. A general form is

$$\Psi = \Psi_{\text{ref}} \exp\left[\frac{E_{act}^{\Psi}}{R}\left(\frac{1}{T_{ref}} - \frac{1}{T}\right)\right] \tag{4}$$

where Ψ_{ref} is a general property value as a reference temperature (T_{ref}) of 25 °C. The activation energy E_{act}^{Ψ} for the anode and cathode exchange current densities, anode and cathode diffusion coefficients, and electrolyte diffusion coefficient and conductivity are 30, 30, 4, 20, 10, and 20 kJ mol^{-1}, respectively [19].

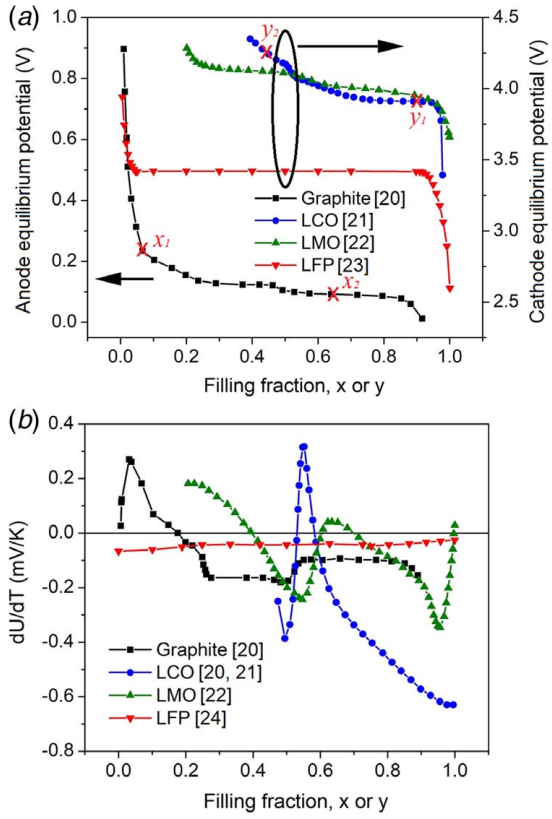

Fig. 2 (*a*) The equilibrium potentials and (*b*) entropy changes of graphite anode and LCO, LMO, and LFP cathodes

3.2 Thermal Model. The battery temperature can be determined from the governing equation of the thermal model,

$$\rho c_p \frac{dT}{dt} = \nabla \cdot (\mathrm{k}\nabla T) + q_{rev} + q_j + q_r \tag{5}$$

where ρ is the density, kg m^{-3}, c_p is the specific heat capacity, J kg^{-1} K^{-1}, k is the thermal conductivity, W m^{-1} K^{-1}, q_{rev}, q_j, and q_r are the reversible, ohmic, and reaction heat sources, respectively. The reversible heat source can be described in the following equation:

$$q_{rev} = \frac{\int_0^{l_n+l_s+l_p} j^{Li} T \frac{\partial U}{\partial T} dx}{l} \tag{6}$$

where l_n, l_s, l_p, and l are the thicknesses of the negative electrode, separator, positive electrode, and entire electrochemical cell, respectively; j^{Li} is the reaction current density, A m^{-3}. The reversible heat is an important contributor to the overall heat generation. It is associated with the entropy change of the active material, and

Table 3 Electrochemical and thermal parameters used in the coupling model

Parameter	Graphite	Separator	LCO	LMO	LFP	Al foil	Copper foil
$l(\mu m)$	34.5[a]	18[a]	26[a]	35[c]	39.5[c]	8[d]	6[d]
$R_s(\mu m)$	5 [26]	–	1 [19]	6.5 [28]	0.0365 [30]	–	–
$D_e(m^2\ s^{-1})$	2.6×10^{-10} [19]	2.6×10^{-10} [19]	2.6×10^{-10} [19]	2.6×10^{-10} [19]	2.6×10^{-10} [19]		
$D_s(m^2\ s^{-1})$	8.86×10^{-15} [21]	–	8.93×10^{-16} [27]	3.98×10^{-14} [28]	8.0×10^{-18} [31]	–	–
ε_s	0.58 [19]	0.5 [26]	0.6[b]	0.559 [28]	0.435 [30]	–	–
ε_e	0.332 [19]	0.5 [26]	0.3[b]	0.33 [28]	0.33 [32]	–	–
$c_{s,max}(mol\ m^{-3})$	31858 [21]	–	49,973 [21]	23,230 [28]	22,806 [30]	–	–
$c_{s,0}(mol\ m^{-3})$	1911[b]	–	44,949[b]	22,068[b]	21,666[b]	–	–
$c_e(mol\ m^{-3})$	1200 [19]	1200 [19]	1200 [19]	1200[b]	1200[b]		
$\sigma(S\ m^{-1})$	100 [19]	–	10 [19]	3.8 [29]	0.005, 0.01, 0.5 [31–33]	–	–
t_+^0	0.363 [19]	0.363 [19]	0.363 [19]	0.363[b]	0.363[b]	–	–
$i_0(A\ m^{-2})$	36 [19]	–	26 [19]	26 [26]	3.18 [34]	–	–
$k(W\ m^{-1}\ K^{-1})$	1.04 [35]	0.15 [37]	1.58 [35]	1.58[b]	1.58[b]	238 [35]	398 [35]
$\rho(kg\ m^{-3})$	1347 [36]	1009 [36]	2500 [37]	2500[b]	2500[b]	2702 [35]	8933 [35]
$c_p(J\ kg^{-1}\ K^{-1})$	1437 [35]	1200[b]	1270 [35]	1269[b]	1269[b]	903 [35]	385 [35]

[a]Measured data.
[b]Estimated data.
[c]Calculated data.
[d]The thicknesses of the current collectors are 1/2 the actual thicknesses since two adjacent electrochemical cells share the current collector.

they are related through the following equation:

$$\Delta S = nF\frac{\partial U}{\partial T} \tag{7}$$

where n is the number of electrons per reaction and equals to 1; F is the Faraday constant and has a value of 96,485 C mol^{-1}. It is common to see the entropy changes in the literature; we thus convert it to the $\partial U/\partial T$ form to make it easier to be used in Eq. (6). The entropy terms of graphite anode, LCO, LMO, and LFP cathodes were collected from the literature and replotted in Fig. 2(*b*) [20–22,24]. The other two heat source terms are ohmic heat q_j and reaction heat q_r, and they are collectively known as the irreversible heat. The expressions of these two heat sources are [41] as follows:

$$q_j = \frac{\int_0^{l_n+l_s+l_p}\left[\sigma^{\text{eff}}\left(\frac{\partial\Phi_s}{\partial x}\right)^2 + k^{\text{eff}}\left(\frac{\partial\Phi_e}{\partial x}\right)^2 + \frac{2k^{\text{eff}}RT}{F}(1-t_+^0)\frac{\partial(\ln c_e)}{\partial x}\frac{\partial\Phi_e}{\partial x}\right]dx}{l} \tag{8}$$

$$q_r = \frac{\int_0^{l_n+l_s+l_p} j^{Li}(\Phi_s - \Phi_e - U)dx}{l} \tag{9}$$

where σ^{eff} and k^{eff} are the effective conductivities of active materials and electrolyte, respectively, in S m^{-1}; R and F are the Faraday's constant (96,487 C mol^{-1}) and universal gas constant (8.3143 J mol^{-1} K^{-1}), respectively; t_+^0 is the transference number of Li^+ ion with respect to the velocity of solvent; c_e is the concentration of Li^+ ion in electrolyte phase, mol m^{-3}. The first term on the right-hand side of Eq. (8) refers to the charge transport in the solid electrode and the last two terms describe the heat from charge transfer in the liquid electrolyte.

In the thermal model, a convection cooling boundary condition is applied to battery surfaces. As an example, the heat dissipation in the x-direction is given as follows:

$$-k\frac{\partial T}{\partial x} = h(T - T_{amb}) \tag{10}$$

where h is the convection heat transfer coefficient, W m^{-2} K^{-1}, T is the battery temperature, and T_{amb} is the ambient temperature.

As described in Sec. 3.1, the cathode thicknesses of LMO and LFP are adjusted to match with the reference graphite anode. As a result, the battery thicknesses in the thermal model are different for the LMO and LFP batteries, 5.7 mm for the LMO battery and 5.96 mm for the LFP battery.

4 Results and Discussion

4.1 Model Validation. The convection heat transfer coefficient at the battery surface is first extracted from model-experimental comparison and then used in the thermal model to validate the coupling model. To extract the heat transfer coefficient, the cooling curve of the LCO pouch battery from an initial temperature of 40 °C to a room temperature of 24 °C was recorded, and it was used to compare with the temperature profile obtained from the thermal model using different heat transfer coefficients. The cooling process can be described by

$$\rho c_p\frac{dT}{dt} = \nabla\cdot(k\nabla T) \tag{11}$$

The density ρ and specific heat capacity c_p of the battery are averaged on a volume basis across the electrochemical cell, while the thermal conductivities in the x-direction and y- and z-directions (Fig. 1(*b*)) are calculated by

$$k_x = \frac{\sum_i l_i}{\sum_i \frac{l_i}{k_i}} \tag{12}$$

$$k_y = k_z = \sum_i \frac{l_i}{l}k_i \tag{13}$$

where l_i and k_i are the thickness and thermal conductivity of each component in the electrochemical cell. The convection heat transfer coefficient value has been fitted (6 W m^{-2} K^{-1}) to match numerical results with experimental measurements, as shown in Fig. 3. Therefore, this coefficient was used in the rest of the simulations.

Figure 4 compares the measured and simulated voltage and temperature curves of the pouch battery at 0.5, 1, and 3 C rates. The root-mean-square errors (RMSEs) of the simulation results are also calculated at an SoC interval of 0.005 and summarized in Table 4. The simulated voltage profiles have similar RMSEs at the tested C rates, and the maximum error occurs at the beginning stages of charges, as shown in Figs. 4(*a*), 4(*c*), and 4(*e*). This error is probably a result of the selected initial Li^+ ion concentration for the anode, and a lower initial voltage can be obtained when having a smaller stoichiometry. However, several trials were conducted, and it was found that the selected initial Li^+ ion concentration is the closest one that can provide good predictions of the voltages at SoCs of greater than 0.1. Regarding the simulated temperature curves, their RMSE increases at higher charging rates. The increased RMSE is possibly caused by the neglected contact

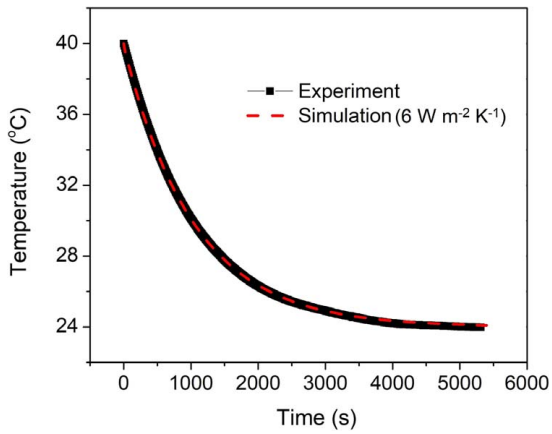

Fig. 3 Comparison of the cooling curves obtained in experiment and simulation

Table 4 RMSEs of the simulation results

C rates (C)	RMSEs of voltage (V)	RMSEs of temperature (°C)
0.5	0.059	0.27
1	0.059	0.34
3	0.056	0.42

electrical resistance between the clamps and battery tabs, which can warm up the battery due to Joule heating, especially at a higher rate. In Figs. 4(*b*), 4(*d*), and 4(*f*), simulated temperatures show bigger discrepancies from the experiments at an SoC of around 0.6. Factors such as the additives used in the electrodes, purity of the active materials, and the varying particle sizes can to some extent lead to the discrepancies.

As shown in Figs. 4(*b*), 4(*d*), and 4(*f*), the battery temperatures drop initially at all charging rates, which is attributed to the endothermic effect of both the graphite anode and LCO cathode. To explain this effect, the lithium stoichiometries of anode and cathode at the beginning of the charging process are labeled in Fig. 2 as x_1 and y_1, respectively. After checking the corresponding values of the entropy changes in Fig. 2(*b*), it is seen that the entropy change is positive in anode and negative in the cathode. Consequently, both electrodes absorb the heat according to Eq. (6), in which the current density is negative in anode and positive in cathode.

4.2 Effect of Cathode Materials. Three common cathodes materials, LCO, LMO, and LFP are compared in this section. In Fig. 5(*a*), the simulated voltage curves of the LCO battery at charge rates of 1 C, 5 C, and 10 C are plotted. It is seen that as the charge rate increases from 1 C to 10 C, the time spent to charge the battery to 4.2 V drops from 3543 s to 252 s. Since the reference battery is designed for fast charging, its thin electrodes facilitate the ion diffusion and only produce a small increase in overpotential, as reflected from the change of the voltage plateaus. The battery eventually attains almost 70% of the total capacity during the 10 C constant rate charge.

In Fig. 5(*b*), the total heat generation rates of the battery with and without considering the reversible heat are plotted in solid and dotted lines, respectively. The total heat without considering the reversible heat part can be regarded as the irreversible heat, and its generation rates are relatively flat during the entire charges. With considering the reversible heat, the total heat generation varies significantly during the charges due to the strong SoC dependency of the reversible heat of the LCO battery. It is seen that the battery has negative heat generation rates at the beginning stage of charges. As charge processes proceed, the heat generation rate reaches 0 W m^{-3}, and the battery reaches a zero heat generation rate earlier at a higher charge rate due to the concentration polarization effect. Thereafter, the total heat generation rate shows a wave shape, which is the combined effect of the anode and cathode entropy changes.

The temperature curves of the battery with and without considering the reversible heat are plotted in Fig. 5(*c*). It is seen that the reversible heat source of the LCO battery is helpful in alleviating the temperature rises during high rate charges. It is noteworthy that although the reversible heat source of the LCO battery is beneficial to the charging process, it will increase the total heat generation during discharges due to the reverse of the current flow. This thermal feature is suitable for future BEV applications, where high-rate charges for convenience and low-rate discharges for long ranges are expected. Since the LCO battery has the disadvantages of high cost, short lifespan, and low heat tolerance [42], material scientists may design novel electrodes by blending other metals, such as nickel, manganese, aluminum, etc. with the LCO electrode, and adjusting the contents of the metals to achieve an overall negative entropy change while ensuring high performance and safety standards.

In Fig. 6, the simulation results of the LMO battery are given. It can be seen that the battery has a similar charging capability as the LCO battery during high rate charges, and it can achieve around 0.7 SoC at the end of the 10 C charge. In comparison, the thermal responses of the LMO battery are different from the LCO battery. Although the heat generation rate and temperature curves excluding the reversible heat are similar to that of the LCO battery, the total heat generation and the temperature are much higher than the LCO battery when considering the reversible heat source, indicating that the overall reversible heat in the LMO plays a positive role in increasing total heat generation. As shown in Fig. 2(*b*), the entropy change of the LMO cathode is negative at most stoichiometries, which means that the positive reversible heat generation of entire battery is mainly attributed to the exothermic behavior of the graphite anode during charges. Research shows that the lithium titanate anode generates less reversible heat than the graphite during charges, but it leads to a relative low operating voltage [43]. Future research could prepare new anode or modify the graphite anode to make them less exothermic during charges to promote the fast-charging technology.

The LFP is a well-commercialized cathode due to its low cost and high safety, but it suffers the drawbacks of low solid-phase diffusion coefficient and poor electrical conductivity. As the data given in Table 3, the relevant parameters are around two orders lower than that of the other two cathodes. To offset the solid-phase diffusion limitation, the LFP active materials are usually prepared in nano-size particles [5,44]. In addition, the LFP cathode can be modified through doping and adding conductive additives to improve the electrical conductivity.

In this part, simulation is first carried out on the LFP battery with a cathode conductivity of 0.005 S m^{-1}, which is close to the conductivity of raw LFP materials and has been used in several articles [31]. The simulation results are shown in Fig. 7. It is seen that the LFP battery can be fully charge at a 1 C rate, but the charged capacity dramatically drops as the charge rate increases, with SoCs of 0.21 and 0.07 at the end of 5 C and 10 C constant rate charges, respectively. Since the LFP cathode is the limiting electrode during the high rate charges, the ratios of the average Li^+ ion concentration over the maximum concentration in the LFP particles at the end of the charge processed are plotted in Fig. 7(*b*), which reveals the Li^+ ion deintercalation ratio on the cathode. At 1 C rate, Li^+ ions are mostly deintercalated from the LFP at the end of charge, and only a small region on the left of the cathode is partially occupied by Li^+ ions. However, when the charge rate increases to 5 C and 10 C, it is seen that only the right region that closes to the current collector releases the Li^+ ions, while most of the cathode is at a Li^+ ion-rich state, which indicates that the poor electrical conductivity impedes the charge reaction to proceed. In Fig. 7(*c*), the irreversible heat generation rate (i.e.,

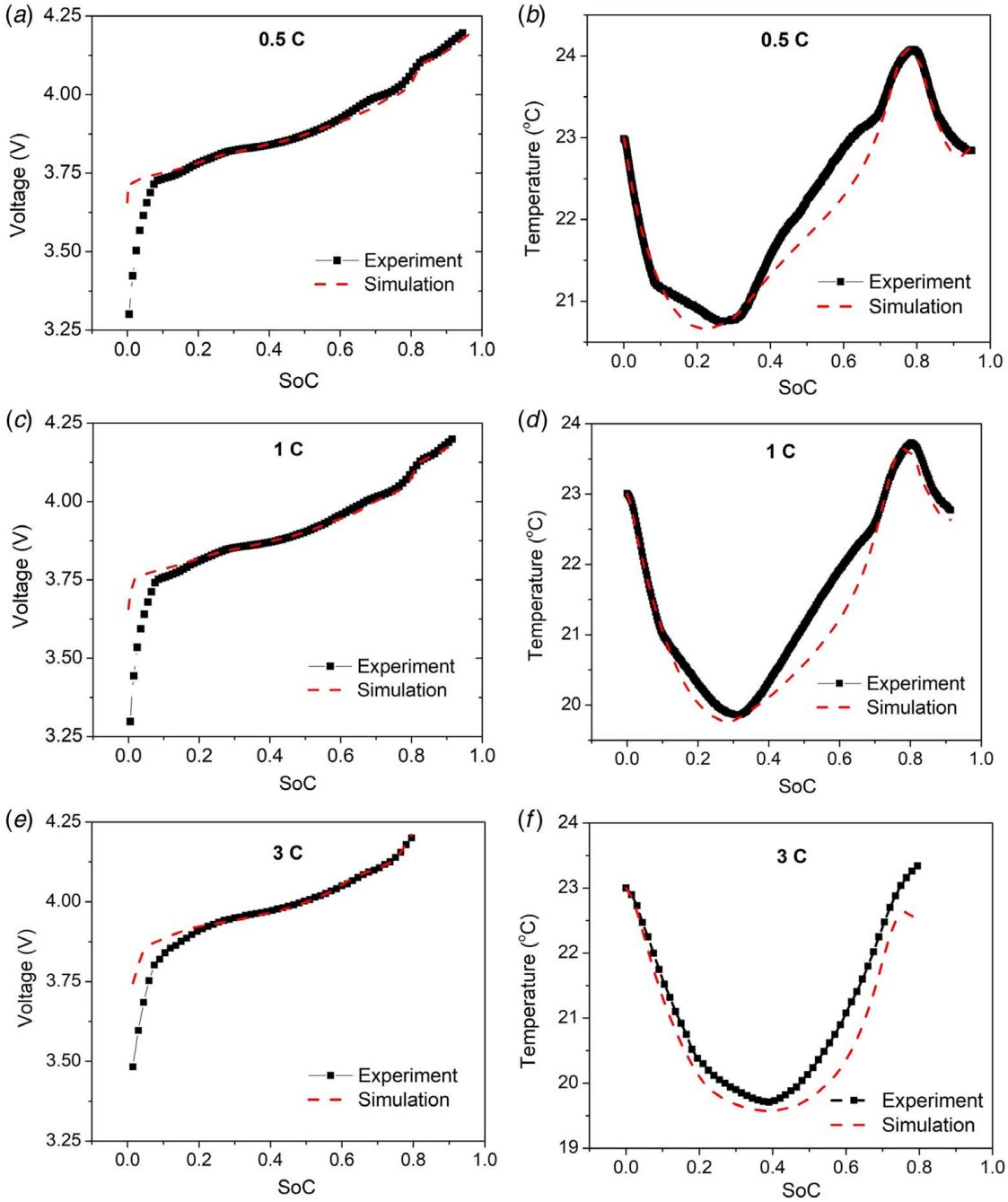

Fig. 4 Comparisons of the experimentally and numerically obtained voltage curves at (*a*) 0.5 C, (*c*) 1 C, and (*e*) 3 C, and temperature curves at (*b*) 0.5 C, (*d*) 1 C, and (*f*) 3 C

w/o reversible heat) and the total heat generation rates are plotted. Different from the LCO and LMO batteries, the reversible heat of the LFP battery contributes only a small fraction of the total heat generation. The reasons for the reduced proportion of reversible heat are two-fold. First, the entropy change of the LFP cathode is flat and close to zero, the graphite anode, therefore, becomes the only contributor to the reversible heat generation. Second, the low conductivity of the LFP cathode significantly intensifies the ohmic heat generation and, therefore, increases the total heat generation and weakens the impact of the reversible heat. As the temperatures shown in Fig. 7(*d*), the maximum temperature of the LFP battery at the end of the 1 C charge is 30.5 C, much higher than that of the LCO and LFP batteries.

To investigate how charge transfer affects the fast charging performance of the LFP battery, a sweep study at 10 C charging rate is carried out by using different cathode conductivities, 0.005, 0.01, and 0.5 S m^{-1}. These values appeared in different LFP battery simulation articles, and they can represent the conductivity of the LFP cathode with different degrees of electrode treatment. As shown in Fig. 8(*a*), the increase of the cathode conductivity is helpful in enhancing the fast-charging capability of the battery, and the battery can be fully charged as the cathode conductivity reaches 0.5 S m^{-1}. Figure 8(*b*) shows the electrical potential on the cathode. It is seen that the cathodes with electrical conductivities of 0.005 S m^{-1} and 0.01 S m^{-1} have uneven potential distributions, where the right end of the cathode reaches the cut-off voltage of 3.6 V while the potential on the left region is still at low levels, indicating the charge transfer hinders the battery from charging at a high rate. As a consequence, the Li^+ ions on the cathodes are poorly deintercalated, as indicated by the curves with the asterisk and

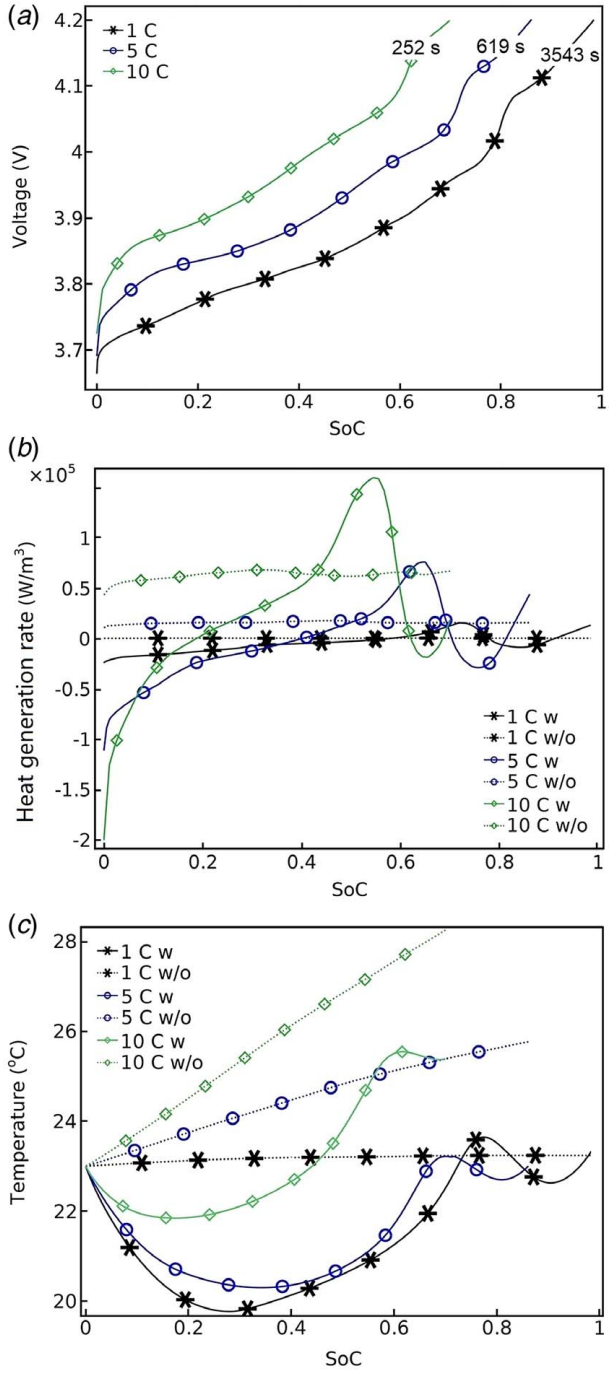

Fig. 5 Simulation results of the LCO battery: (*a*) voltage curves, (*b*) total heat generation rates with and without considering the reversible heat, and (*c*) temperature curves with and without considering the reversible heat

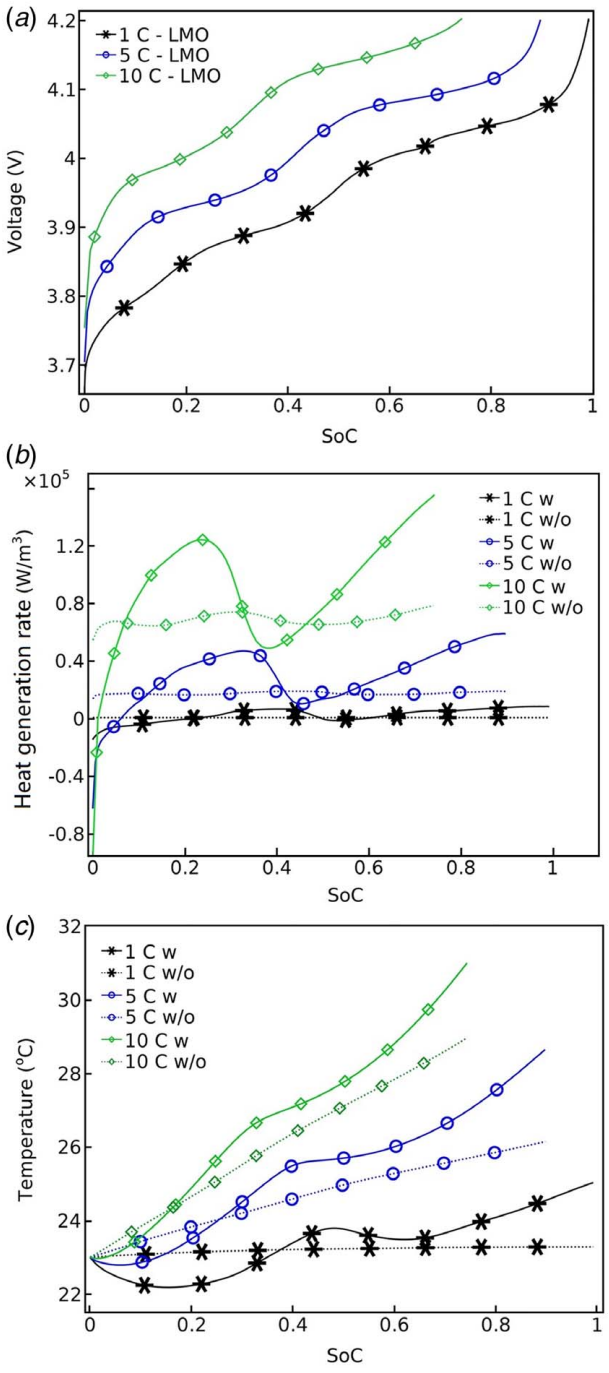

Fig. 6 Simulation results of the LMO battery: (*a*) voltage curves, (*b*) total heat generation rates with and without considering the reversible heat, and (*c*) temperature curves with and without considering the reversible heat

circle symbols in Fig. 8(*c*). The increase of the cathode conductivity can also alleviate the thermal responses of the battery due to the reduced irreversible heat generation. As shown in Fig. 8(*d*), at the 10 C charge rate, the heat generation rate of the LFP battery fluctuated at 10^5 W m^{-3}, close to that of the LMO battery.

4.3 Effect of Electrode Parameters. The fast-charging capability of Li-ion batteries is affected by electrochemical parameters including the ion diffusivity in electrolyte and electrodes as well as the electrical conductivity of electrodes, which are directly related to the ion and charge transfers in batteries. Approaches have been developed to improve the ion and charge transfers, for example, through the preparations of weakly bound solvation structure [45], novel anodes [46], and modified electrodes [47]. In Sec. 4.2, the effect of LFP conductivity in affecting the fast-charging performance of Li-ion batteries was discussed. In this section, two geometrical parameters of electrochemical cell, electrode thickness and solid electrode particle size, are investigated on the LCO battery. These parameters are selected because they are related to the ion diffusion in electrode level and particle level, respectively, and they can easily be adjusted by battery manufacturers during the electrode coating stage and active material grinding stage.

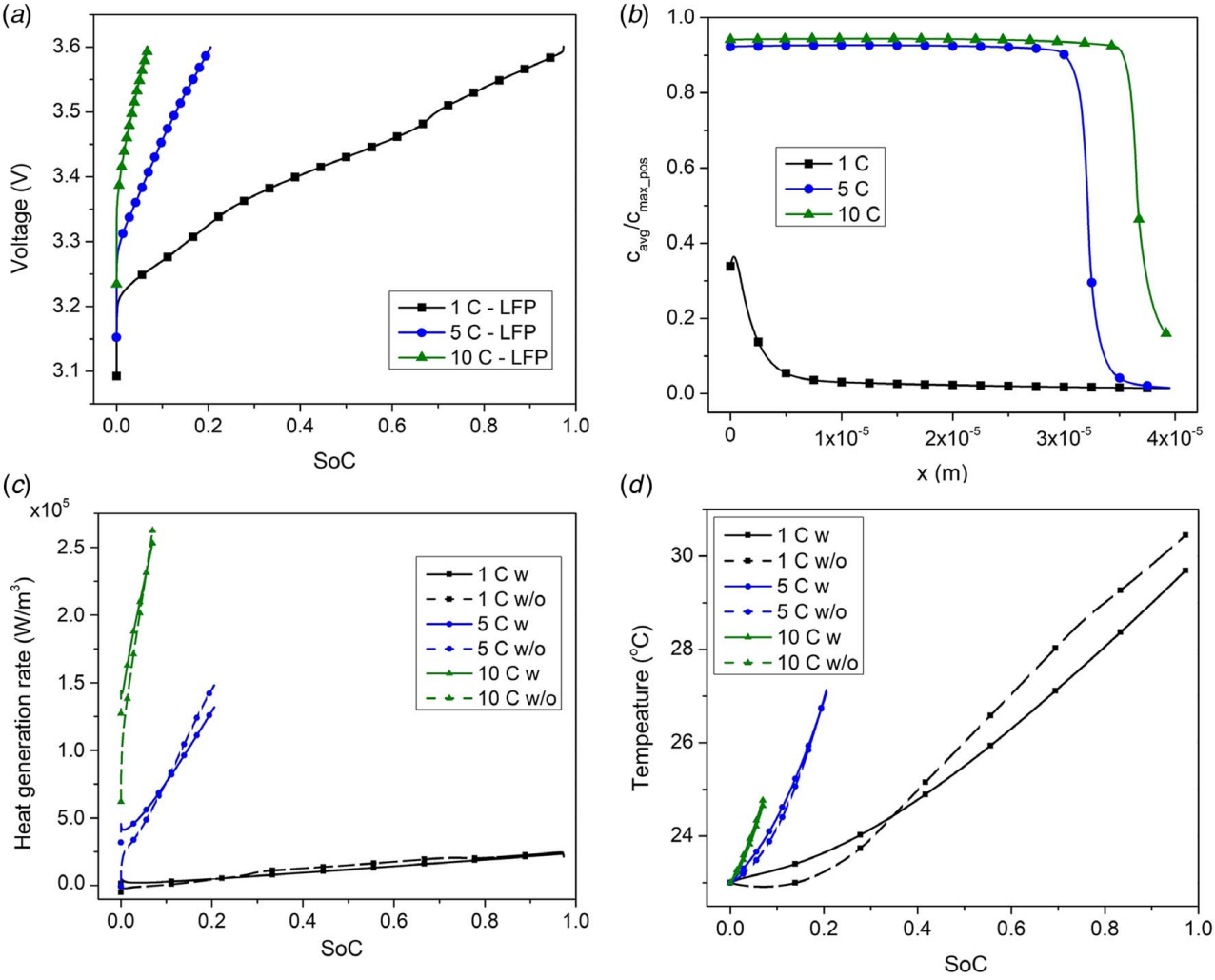

Fig. 7 Simulation results of the LFP battery: (*a*) voltage curves, (*b*) cathode deintercalation ratio at the end of charges, (*c*) heat generation rates with and without considering the reversible heat, and (*d*) temperature curves with and without considering the reversible heat

As the parameters shown in Table 3, the cathode thickness of the high-drain LCO battery is 26 μm, which is already thin enough to undertake the high current, and a further reduction in the thickness will notably decrease the energy density of the battery. Therefore, the thicknesses of the electrodes are increased by 50%, 100%, and 150% to study how diffusion in electrode level can affect the fast-charging performance of the battery. The current densities applied to the cell are also increased by the same percentages to match up with the thicker electrodes. In Fig. 9, the voltage and temperature curves of the LCO batteries during 10 C rate charges are plotted. It is seen that the increase of electrode thickness induces higher voltage plateaus and lower charged capacities. The increased overpotential also triggers intensive thermal responses due to the significantly increased ohmic heat generation [48]. Consequently, the battery temperature increases at higher rates in batteries with thicker electrodes, as shown in Fig. 9(*b*).

To explain the causes of the reduction of charged capacity, the electrolyte potential in the electrochemical cell and the ratio of average Li^+ ion concentration to the maximum Li^+ ion concentration in graphite particles at the end of charges are shown in Figs. 10(*a*) and 10(*b*), respectively. Because only the slope of the curves and potential difference along the electrochemical cell are concerned, for clearer comparisons, the electrolyte potential curves are arbitrarily relocated. As shown in Fig. 10(*a*), with the increase of the anode and cathode thicknesses, the slope of the electrolyte potential profile and the potential difference across the cell become significantly bigger. For example, the electrolyte potential difference of electrochemical cell using the thinnest electrodes is within 0.1 V, while this value soars up to 0.432 V in the cell using the thickest electrodes, indicating a severer concentration polarization. The concentration polarization is an important contributing factor related to the performance degradation of Li-ion batteries, since it can lead to the underutilization of active materials in electrodes. In Fig. 10(*b*), the anode utilization ratio is provided since Li^+ ions intercalate into the anode during the charging process. It is seen that the anode utilization ratio is the highest in the thin-electrode battery and the ratio drops as the electrodes become thicker. It is also observed that the right regions of the anodes are better occupied in receiving the Li^+ ions. This is because during the charging process, Li^+ ions are generated in the cathode and diffuse to the anode from its right side, where the electrochemical reactions will first take place. Due to the large charge current, most of the ions are involved in the electrochemical reactions at the right region of the anode prior to diffuse to the left region, and eventually, the polarization is developed and the cut-off voltage is reached.

Lithium plating is one of the potential safety issues, which is associated with the fast charging. The generated lithium dendrites can grow gradually and penetrate separators and cause an internal short circuit. During high-rate charges, the Li^+ ion intercalation reaction in the anode is nonuniform, which can cause some regions, especially those close to the separator, have excess Li^+

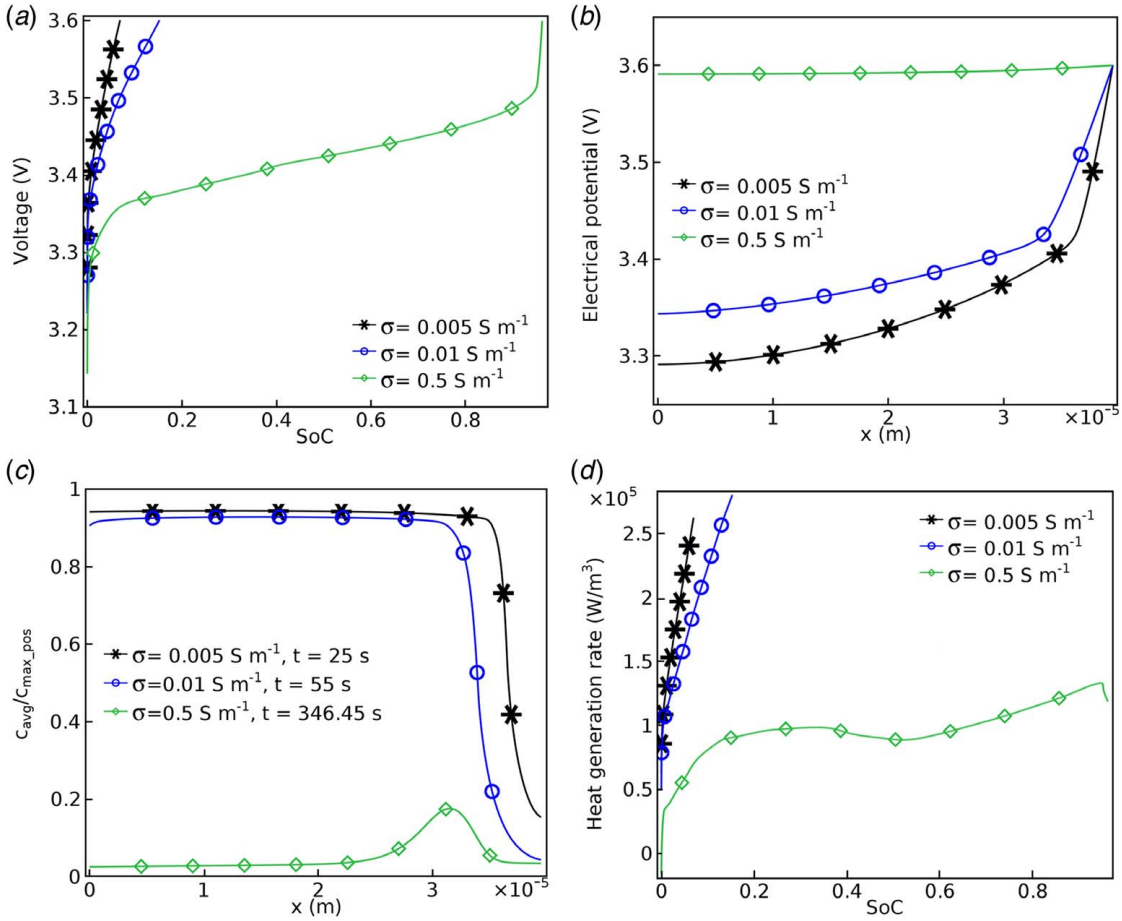

Fig. 8 Simulation results of the LFP battery with different cathode conductivities: (*a*) voltage curves, (*b*) cathode electrical potential at the end of 10 C charges, (c) cathode deintercalation ratio at the end of 10 C charges, and (*d*) heat generation rates

ions participated the reaction. Consequently, the overpotential at those regions can fall below the potential to produce the lithium dendrites. To investigate the lithium plating behavior in the batteries that employ electrodes with different thicknesses, the overpotential on anode $\phi_s - \phi_l$ is plotted along the anodes for the cells. As compared with Eq. (1), the equilibrium potential for lithium plating is taken as zero because the potential is measured with respect to a lithium metal reference. In Fig. 11, it is seen that the cells using 2 and 2.5 times the original electrode thicknesses experience negative overpotentials at the right ends of the anodes. Anticipated lithium deposition could occur since a negative overpotential indicates the onset of the side reaction [49].

Nanotechnology can significantly improve the energy and power densities of Li-ion batteries. Many research works published by Cui's research group have demonstrated the advantages of using nano-scale anodes and cathodes in Li-ion batteries [50–52]. The discussion in the Sec. 4.2 on the LFP battery also illustrates that a smaller active material size can offset the low diffusivity of the LFP.

To study the effect of electrode particle size on the fast-charging performance of Li-ion batteries, the particle radius of the LCO battery electrodes is adjusted to 0.25, 0.5, 2, and 4 times of the original sizes, and charging simulations at a 10 C rate are carried out on the batteries. The voltage curves are plotted in Fig. 12(*a*). It is seen that the charge process is terminated earlier in batteries with larger particles. For example, as the particle sizes increase to four times of the original sizes, less than 10% capacity can be charged into the battery. The large particles can lead to poor utilization of the active materials and reduce the charged capacity consequently. To investigate the diffusion limitation and active material utilization of the cells, the ratio of surface Li^+ ion concentration to maximum Li^+ ion concentration and the ratio of average Li^+ ion concentration to maximum Li^+ ion concentration are plotted for the cells that use the largest particles and smallest particles, as shown in Fig. 12(*b*). With larger particles used, significant concentration differences are observed between the particle surfaces and interiors as the arrows indicate. The high surface concentration ratio of the large particle anode creates an illusion of well-intercalated graphite, but as we look at the average concentration ratio, it is at an extremely low level, indicating an underutilization of the anode. Therefore, the particle level ion diffusion becomes the predominant factor that deteriorates the fast charging performance. In comparison, as the particle size drops to one-fourth of the original size, the surface and interior Li^+ ion concentration ratio curves are basically overlapped, and the concentration polarization in particle level is dramatically reduced. It is also notable that a further reduction of the particle size will not show an evident improvement in the fast-charging capability of the battery at a 10 C rate since the particle-level diffusion is no longer the limiting factor. Figures 12(*c*) and 12(*d*) shows the temperature profiles and total heat generation rates of the batteries. Batteries with smaller particles are found to have lower minimum temperatures, which is because the sufficient use of the LCO cathode extends the heat absorption stage, as shown in Fig. 12(*d*).

In Fig. 13, the lithium plating overpotentials on the anodes are plotted. The overpotential decreases as the particle size increases, and a negative overpotential is found on the anode that uses the largest active particles. Previous research showed that the lithium plating can be minimized by increasing the excess anode percentage, but this approach reduces the energy density of batteries [49]. Overall, batteries targeted for different applications can be

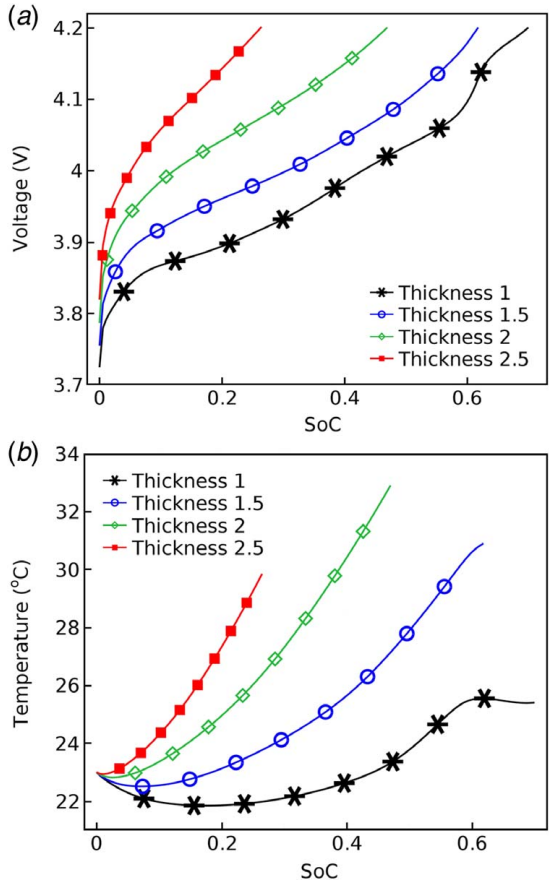

Fig. 9 Simulated (*a*) voltage and (*b*) temperature curves of the LCO batteries with different electrode thicknesses during 10 C charges

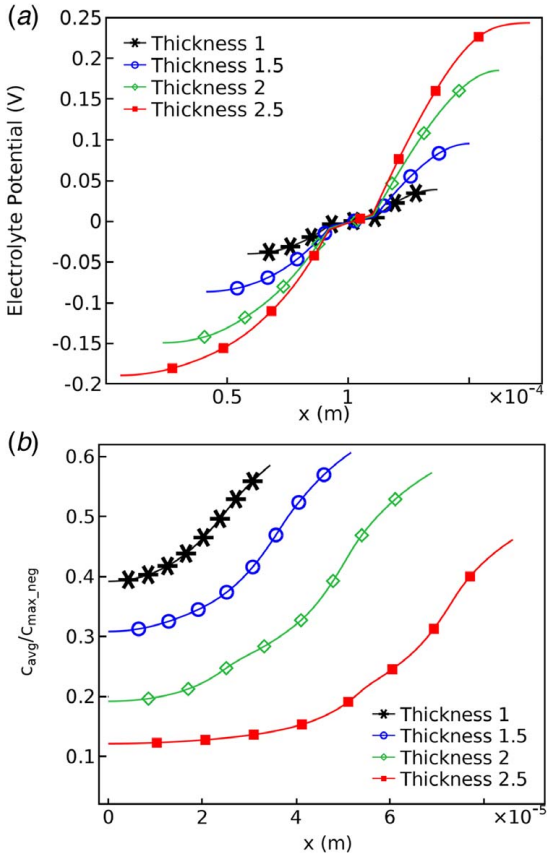

Fig. 10 Plots of (*a*) the electrolyte potentials along the electrochemical cells and (*b*) anode utilization ratios of the LCO batteries with different electrode thicknesses at the end of 10 C charges

designed with different excess anode percentages and/or particle sizes and/or electrode thicknesses to meet individual charge/discharge requirements.

5 Conclusion

In this paper, an electrochemical-thermal coupled charging model is implemented to study the effects of cathode materials and electrode parameters on the fast-charging performance of Li-ion batteries. The voltage and temperature profiles of a high-drain pouch LCO battery are recorded and used to validate the coupling model. Two other batteries that use the LMO and LFP cathodes are compared with the reference LCO battery in their electrochemical and thermal behaviors. Among the batteries, the LCO and LMO batteries can be charged with similar capacities during high rate charges, while the LFP battery shows the worst fast charging performance especially at high rates due to its low electrical conductivity of the raw cathode material, which, however, can be significantly improved by electrode modification, e.g., doping and adding additives. With having different entropy changes, the LCO, LMO, and LFP batteries are compared in terms of their thermal responses during high rate charges. Among the batteries, the reversible heat of the LCO battery shows an overall endothermic effect and helps alleviate the temperature rises during the charging processes, while the reversible heat of the LMO and LFP batteries plays a negative role. As a result, the LCO battery has a better thermal response than the other two batteries during fast charging.

The diffusion limitations of fast charging at the electrode and active particle levels are also investigated by adjusting the electrode thicknesses and particle radiuses, respectively. Thicker electrodes lengthen the diffusion path of ions and intensify the concentration polarization, and eventually lead to the earlier stop of the charging process. Moreover, a thicker anode also poses a higher risk of lithium plating during high rate charges. Active material size can significantly affect the Li^+ ion diffusion on the particle level due to the low ion diffusivity in the solid phase. Large particles can lead to the underutilization of active materials since a high Li^+ ion concentration is reached at the surface of particles that terminates the charging process before the interiors of particles are

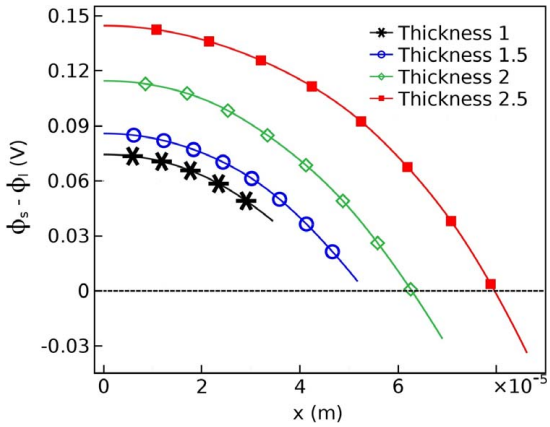

Fig. 11 Anode lithium plating overpotential curves of LCO batteries with different electrode thicknesses at the end of 10 C charges

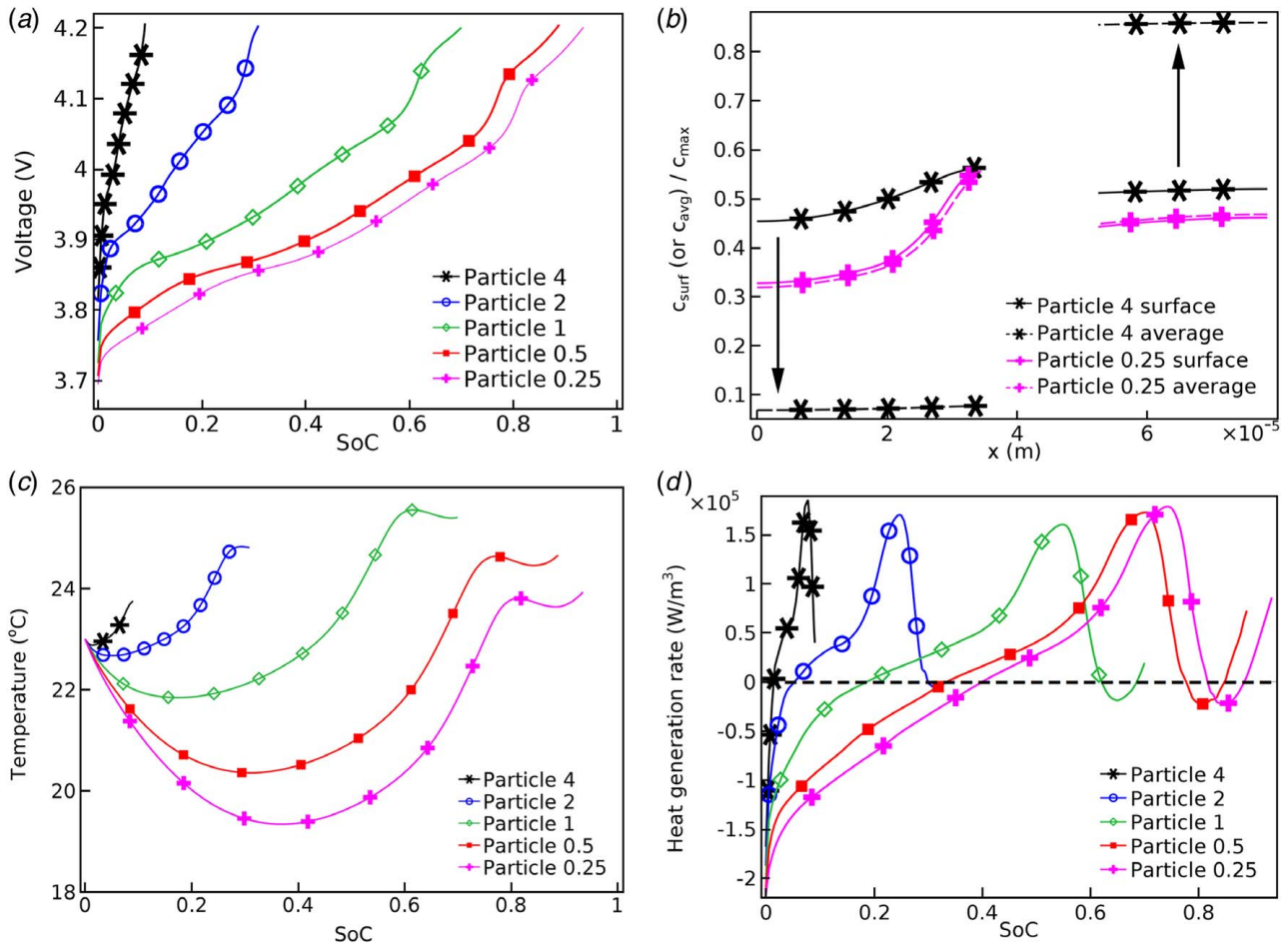

Fig. 12 Simulation results of the batteries using electrodes of different particle sizes during 10 C charges: (*a*) voltage curves, (*b*) anode utilization ratios of selected batteries at the end of charges, (c) temperature curves, and (*d*) heat generation rates

well filled by Li^+ ions. It is also found that lithium plating is prone to appear on anodes with large active particles.

Overall, the electrochemical and thermal performance of Li-ion batteries during fast charging can be affected by factors including the cathode chemistries, electrode thickness, secondary particle sizes of active materials, electrical conductivity of electrodes, etc. The results of this work will facilitate future studies on developing adequate cathodes and selecting optimum parameters for Li-ion batteries used in fast-charging applications.

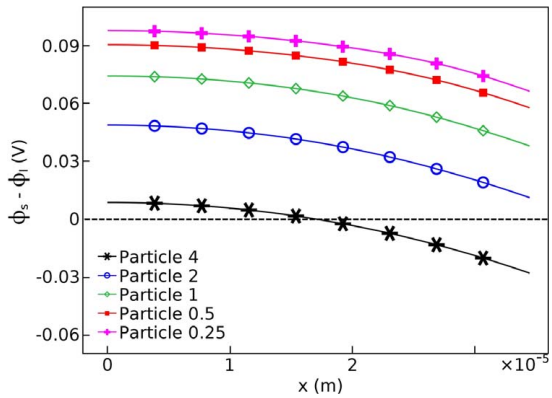

Fig. 13 Anode lithium plating overpotential curves of LCO batteries with different active particle sizes

Acknowledgment

The authors sincerely thank the fellowship from the National Sciences and Engineering Research Council (NSERC) of Canada and Carleton University.

Nomenclature

- k = conductivity of different components inside cell, W m^{-1} K^{-1}
- c = volume-averaged concentration of lithium in a phase, mol m^{-3}
- h = convective heat transfer coefficient, W m^{-2} K^{-1}
- i = current density, A m^{-2}
- k = conductivity of electrolyte, S m^{-1}
- l = thickness or thickness of electrochemical cell, m
- n = number of electrons per reaction
- r = radial coordinate, m
- t = time, s
- x = negative electrode solid-phase stoichiometry or x-axis
- y = positive electrode solid-phase stoichiometry or y-axis
- z = z-axis
- D = diffusion coefficient of lithium species, m^2 s
- F = Faraday's constant, 96,487 C mol^{-1}
- S = entropy, J K^{-1}
- T = temperature, K
- U = open circuit potential, V
- a_s = active surface area per electrode unit volume, m^2 m^{-3}
- c_p = specific heat capacity of component inside cell, J kg^{-1} K^{-1}

$c_{s,max}$ = maximum concentration of lithium in solid phase, mol m^{-3}
$c_{s,0}$ = initial concentration of lithium in solid phase, mol m^{-3}
i_0 = exchange current density, A m^{-2}
l_n = thickness of negative electrode, m
l_p = thickness of positive electrode, m
l_s = thickness of separator, m
q_j = volumetric ohmic heat generation rate, W m^{-3}
q_r = volumetric reaction heat generation rate, W m^{-3}
q_{rev} = volumetric reversible heat generation rate, W m^{-3}
E_{act} = activation energy, J mol^{-1}
R_s = radius of solid particles, m
j^{Li} = reaction current density, A m^{-3}
t_+^0 = transference number of lithium-ion with respect to the velocity of solvent

Greek Symbols

ε = volume fraction of a phase
η = surface overpotential of an electrode reaction, V
ρ = density, kg m^{-3}
σ = electrical conductivity of solid active materials in an electrode, S cm^{-1}
Φ = electrical potential in a phase, V
Ψ = general property value

Subscripts

amb = ambient
e = electrolyte phase
ref = with respect to a reference state
s = solid phase

Superscript

eff = effective value

References

[1] Meintz, A., Zhang, J., Vijayagopal, R., Kreutzer, C., Ahmed, S., Bloom, I., Burnham, A., Carlson, R. B., Dias, F., Dufek, E. J., Francfort, J., Hardy, K., Jansen, A. N., Keyser, M., Markel, A., Michelbacher, C., Mohanpurkar, M., Pesaran, A., Scoffield, D., Shirk, M., Stephens, T., and Tanim, T., 2017, "Enabling Fast Charging—Vehicle Consideration," J. Power Sources, **367**, pp. 216–227.

[2] Burnham, A., Dufek, E. J., Stephens, T., Francfort, J., Michelbacher, C., Carlson, R. B., Zhang, J., Vijayagopal, R., Dias, F., Mohanpurkar, M., Scoffield, D., Hardy, K., Shirk, M., Hovsapian, R., Ahmed, S., Bloom, I., Jansen, A. N., Keyser, M., Kreuzer, C., Markel, A., Meintz, A., Pesaran, A., and Tanim, T. R., 2017, "Enabling Fast Charging—Infrastructure and Economic Considerations," J. Power Sources, **367**, pp. 237–249.

[3] Ahmed, S., Bloom, I., Jansen, A. N., Tanim, T., Dufek, E. J., Pesaran, A., Burnham, A., Carlson, R. B., Dias, F., Hardy, K., Keyser, M., Kreuzer, C., Markel, A., Meintz, A., Michelbacher, C., Mohanpurkar, M., Nelson, P. A., Robertson, D. C., Scoffield, D., Shirk, M., Stephens, T., Vijayagopal, R., and Zhang, J., 2017, "Enabling Fast Charging—A Battery Technology gap Assessment," J. Power Sources, **367**, pp. 250–262.

[4] Keyser, M., Pesaran, A., Li, Q., Santhanagopalan, S., Smith, K., Wood, E., Ahmed, S., Bloom, I., Dufek, E., Shirk, M., Meintz, A., Kreuzer, C., Michelbacher, C., Burnham, A., Stephens, T., Francfort, J., Carlson, B., Zhang, J., Vijayagopal, R., Hardy, K., Dias, F., Mohanpurkar, M., Scoffield, D., Jansen, A. N., Tanim, T., and Markel, A., 2017, "Enabling Fast Charging—Battery Thermal Considerations," J. Power Sources, **367**, pp. 228–236.

[5] Li, Y., El Gabaly, F., Ferguson, T. R., Smith, R. B., Bartelt, N. C., Sugar, J. D., Fenton, K. R., Cogswell, D. A., Kilcoyne, A. L. D., Tyliszczak, T., Bazant, M. Z., and Chueh, W. C., 2014, "Current-induced Transition From Particle-by-Particle to Concurrent Intercalation in Phase-Separating Battery Electrodes," Nat. Mater., **13**(12), pp. 1149–1156.

[6] Colclasure, A. M., Dunlop, A. R., Trask, S. E., Polzin, B. J., Jansen, A. N., and Smith, K., 2019, "Requirements for Enabling Extreme Fast Charging of High Energy Density Li-ion Cells While Avoiding Lithium Plating," J. Electrochem. Soc., **166**(8), pp. A1412–A1424.

[7] Takami, N., Ise, K., Harada, Y., Iwasaki, T., Kishi, T., and Hoshina, K., 2018, "High-energy, Fast-Charging, Long-Life Lithium-ion Batteries Using $TiNb_2O_7$ Anodes for Automotive Applications," J. Power Sources, **396**, pp. 429–436.

[8] Tsai, H. L., Hsieh, C. T., Li, J., and Gandomi, Y. A., 2018, "Enabling High Rate Charge and Discharge Capability, low Internal Resistance, and Excellent Cyclability for Li-Ion Batteries Utilizing Graphene Additives," Electrochim. Acta, **273**, pp. 200–207.

[9] Kim, D. S., Kim, Y. E., and Kim, H., 2019, "Improved Fast Charging Capability of Graphite Anodes via Amorphous Al_2O_3 Coating for High Power Lithium ion Batteries," J. Power Sources, **422**, pp. 18–24.

[10] Yin, Y., Hu, Y., Choe, S. Y., Cho, H., and Joe, W. T., 2019, "New Fast Charging Methods of Lithium-ion Batteries Based on a Reduced Order Electrochemical Model Considering Side Reaction," J. Power Sources, **423**, pp. 367–379.

[11] Zhao, R., Zhang, S., Gu, J., and Liu, J., 2016, "Modeling the Electrochemical Behaviors of Charging Li-Ion Batteries With Different Initial Electrolyte Salt Concentrations," Int. J. Energy Res., **40**(8), pp. 1085–1092.

[12] Fang, H., Depcik, C., and Lvovich, V., 2018, "Optimal Pulse-Modulated Lithium-Ion Battery Charging: Algorithms and Simulation," J. Energy Storage, **15**, pp. 359–367.

[13] Zhang, C., Jiang, J., Gao, Y., Zhang, W., Liu, Q., and Hu, X., 2017, "Charging Optimization in Lithium-ion Batteries Based on Temperature Rise and Charge Time," Appl. Energy, **194**, pp. 569–577.

[14] Chu, Z., Feng, X., Ouyang, M., Wang, Z., Lu, L., Li, J., and Han, X., 2017, "Optimal Charge Current of Lithium Ion Battery," Energy Procedia, **142**, pp. 1867–1873.

[15] von Lüders, C., Keil, J., Webersberger, M., and Jossen, A., 2019, "Modeling of Lithium Plating and Lithium Stripping in Lithium-Ion Batteries," J. Power Sources, **414**, pp. 41–47.

[16] Song, M., and Choe, S. Y., 2019, "fast and Safe Charging Method Suppressing Side Reaction and Lithium Deposition Reaction in Lithium Ion Battery," J. Power Sources, **436**, p. 226835.

[17] Viswanathan, V. V., Choi, D., Wang, D., Xu, W., Towne, S., Williford, R. E., Zhang, J.-G., Liu, J., and Yang, Z., 2010, "Effect of Entropy Change of Lithium Intercalation in Cathodes and Anodes on Li-Ion Battery Thermal Management," J. Power Sources, **195**(11), pp. 3720–3729.

[18] Mao, C., Ruther, E. E., Li, J., Du, Z., and Belharouak, I., 2018, "Identifying the Limiting Electrode in Lithium ion Batteries for Extreme Fast Charging," Electrochem. Commun., **97**, pp. 37–41.

[19] Smith, K., and Wang, C. Y., 2006, "Power and Thermal Characterization of a Lithium-Ion Battery Pack for Hybrid-Electric Vehicles," J. Power Sources, **160**(1), pp. 662–673.

[20] Thomas, K. E., and Newman, J., 2003, "Heats of Mixing and of Entropy in Porous Insertion Electrodes," J. Power Sources, **119–121**, pp. 844–849.

[21] Kumaresan, K., Sikha, G., and White, R. E., 2008, "Thermal Model for a Li-ion Cell," J. Electrochem. Soc., **155**(2), pp. A164–A171.

[22] Yazami, R., Reynier, Y., and Fultz, B., 2006, "Entropymetry of Lithium Intercalation in Spinel Manganese Oxide: Effect of Lithium Stoichiometry," ECS Trans., **1**(26), pp. 87–96.

[23] Yamada, A., Koizumi, H., Nishimura, S.-i., Sonoyama, N., Kanno, R., Yonemura, M., Nakamura, T., and Kobayashi, Y., 2006, "Room-temperature Miscibility gap in Li_xFePO_4," Nat. Mater., **5**(5), pp. 357–360.

[24] Jalkanen, K., Aho, T., and Vuorilehto, K., 2013, "Entropy Change Effects on the Thermal Behaviors of a $LiFePO_4$/Graphite Lithium-ion Cell at Different States of Charge," J. Power Sources, **243**, pp. 354–360.

[25] Doyle, M., Newman, J., Gozdz, A. S., Schmulz, C. N., and Tarascon, J. M., 1996, "Comparison of Modeling Predictions with Experimental Data From Plastic Lithium ion Cells," J. Electrochem. Soc., **143**(6), pp. 1890–1903.

[26] Ender, M., Joos, J., Weber, A., and Ivers-Tiffée, E., 2014, "Anode Microstructures From High-Energy and High-Power Lithium-Ion Cylindrical Cells Obtained by X-ray Nano-Tomography," J. Power Sources, **269**, pp. 912–919.

[27] Xia, H., Meng, Y. S., Lu, L., and Ceder, G., (2007), "Electrochemical Behavior and Li Diffusion Study of LiCoO2 Thin Film Electrodes Prepared by PLD," http://hdl.handle.net/1721.1/35827, last accessed: 08/06/2019.

[28] Appiah, W. A., Park, J., Byun, S., Ryou, M. H., and Lee, Y. M., 2016, "A Mathematical Model for Cyclic Aging of Spinel $LiMn_2O_4$/Graphite Lithium-Ion Cells," J. Electrochem. Soc., **163**(13), pp. A2757–A2767.

[29] Ye, Y., Shi, Y., Cai, N., Lee, J., and He, X., 2012, "Electro-Thermal Modeling and Experimental Validation for Lithium Ion Battery," J. Power Sources, **199**, pp. 227–238.

[30] Safari, M., and Delacourt, C., 2011, "Mathematical Modeling of Lithium Iron Phosphate Electrode: Galvanostatic Charge/Discharge and Path Dependence," J. Electrochem. Soc., **158**(2), pp. A63–A73.

[31] Srinivasan, V., and Newman, J., 2004, "Discharge Model for the Lithium Iron-Phosphate Electrode," J. Electrochem. Soc., **151**(10), pp. A1517–A1529.

[32] Li, J., Cheng, Y., Ai, L., Jia, M., Du, S., Yin, B., Woo, S., and Zhang, H., 2015, "3D Simulation on the Internal Distributed Properties of Lithium-Ion Battery With Planar Tabbed Configuration," J. Power Sources, **293**, pp. 993–1005.

[33] Xu, M., Zhang, Z., Wang, X., Jia, L., and Yang, L., 2015, "A Pseudo Three-Dimensional Electrochemical-Thermal Model of a Prismatic $LiFePO_4$ Battery During Discharge Process," Energy, **80**, pp. 303–317.

[34] Thorat, I. V., Joshi, T., Zaghib, K., Harb, J. N., and Wheeler, D. R., 2011, "Understanding Rate-Limiting Mechanism in $LiFePO_4$ Cathodes for Li-Ion Batteries," J. Electrochem. Soc., **158**(11), pp. A1185–A1193.

[35] Taheri, P., Yazdanpour, M., and Bahrami, M., 2013, "Transient Three-Dimensional Thermal Model for Batteries With Thin Electrodes," J. Power Sources, **243**, pp. 280–289.

[36] Wu, B., Yufit, V., Marinescu, M., Offer, G. J., Martinez-Botas, R. F., and Brandon, N. P., 2013, "Coupled Thermal-Electrochemical Modeling of Uneven Heat Generation in Lithium-Ion Battery Packs," J. Power Sources, **243**, pp. 544–554.

[37] Zavalis, T. G., Behm, M., and Lindbergh, G., 2012, "Investigation of Short-Circuit Scenarios in a Lithium-Ion Battery Cell," J. Electrochem. Soc., **159**(6), pp. A848–A859.

[38] Guzman, G., Vazquez-Arenas, J., Ramos-Sanchez, G., Bautista-Ramirez, M., and Gonzalez, I., 2017, "Improved Performance of $LiFePO_4$ Cathode for Li-Ion Batteries Through Percolation Studies," Electrochim. Acta, **247**, pp. 451–459.
[39] Li, Y., Qi, F., Guo, H., Guo, Z., Li, M., and Wu, W., 2019, "Characteristics Investigation of an Electrochemical-Thermal Coupled Model for a $LiFePO_4$/Graphene Hybrid Cathode Lithium-Ion Battery," Case Stud. Therm. Eng., **13**, p. 100387.
[40] Satyavani, T., Kiran, B., Kumar, R., Kumar, V. R., and Naidu, A. S., and V, S., 2016, "Effect of Particle Size on dc Conductivity, Activation Energy and Diffusion Coefficient of Lithium Iron Phosphate in Li-ion Cells," Eng. Sci. Technol. Int. J., **19**(1), pp. 40–44.
[41] Zhao, R., Gu, J., and Liu, J., 2014, "An Investigation on the Significance of Reversible Heat to the Thermal Behavior of Lithium Ion Battery Through Simulations," J. Power Sources, **266**, pp. 422–432.
[42] Nitta, N., Wu, F., Lee, J. T., and Yushin, G., 2015, "Li-ion Battery Materials: Present and Future," Mater. Today, **18**(5), pp. 252–264.
[43] Lu, W., Belharouak, I., Liu, J., and Amine, K., 2007, "Thermal Properties of $Li_{4/3}Ti_{5/3}O_4$/$LiMn_2O_4$ Cell," J. Power Sources, **174**(2), pp. 673–677.
[44] Eftekhari, A., 2017, "$LiFePO_4$/C Nanocomposites for Lithium-Ion Batteries," J. Power Sources, **343**, pp. 395–411.
[45] Ong, M. T., Verners, O., Draeger, E. W., van Duin, A. C. T., Lordi, V., and Pask, J. E., 2015, "Lithium ion Solvation and Diffusion in Bulk Organic Electrolytes From First-Principles and Classical Reactive Molecular Dynamics," J. Phys. Chem. B, **119**(4), pp. 1535–1545.
[46] Lee, Y. S., and Ryu, K. S., 2017, "Study of the Lithium Diffusion Properties and High Rate Performance of $TiNb_6O_{17}$ as an Anode in Lithium Secondary Battery," Sci. Rep, **7**(1), p. 16617.
[47] Park, C. K., Park, S. B., Oh, S. H., Jang, H., and Cho, W. I., 2011, "Li ion Diffusivity and Improved Electrochemical Performances of the Carbon Coated $LiFePO_4$," Bull. Korean Chem. Soc, **32**(3), pp. 836–840.
[48] Zhao, R., Liu, J., and Gu, J., 2015, "The Effects of Electrode Thickness on the Electrochemical and Thermal Characteristics of Lithium ion Battery," Appl. Energy, **139**, pp. 220–229.
[49] Arora, P., Doyle, M., and White, R. E., 1999, "Mathematical Modeling of the Lithium Deposition Overcharge Reaction in Lithium-Ion Batteries Using Carbon-Based Negative Electrodes," J. Electrochem. Soc., **146**(10), pp. 3543–3553.
[50] Kim, D. K., Muralidharan, P., Lee, H.-W., Ruffo, R., Yang, Y., Chan, C. K., Peng, H., Huggins, R. A., and Cui, Y., 2008, "Spinel $LiMn_2O_4$ Nanorods as Lithium Ion Battery Cathodes," Nano Lett., **8**(11), pp. 3948–3952.
[51] Chan, C. K., Peng, H., Liu, G., Mcllwrath, K., Zhang, X. F., Huggins, R. A., and Cui, Y., 2008, "High-performance Lithium Battery Anodes Using Silicon Nanowires," Nat. Nanotechnol., **3**(1), pp. 31–35.
[52] Wu, H., and Cui, Y., 2012, "Designing Nanostructured Si Anodes for High Energy Lithium Ion Batteries," Nano Today, **7**(5), pp. 414–429.